Russian Journal of Earth Sciences

A New Version of Parametrization of Orographic Waves: Dynamic and Thermal Effects in the SOCOL3 Model

A. V. Koval[1,2*], N. M. Gavrilov[1], V. A. Zubov[1,3], E. V. Rozanov[1,4], and A. S. Fadeev[1]

[1]Saint Petersburg State University, Saint Petersburg, Russia
[2]Russian State Hydrometeorological University, Saint Petersburg, Russia
[3]Voeikov Main Geophysical Observatory, Saint Petersburg, Russia
[4]Davos Physics and Meteorological Observatory/World Radiation Center (PMOD/WRC), Davos, Switzerland
* **Correspondence to:** Andrey Koval, a.v.koval@spbu.ru

Abstract: Orographic gravity waves (OGW) have a significant impact on the global atmospheric circulation, providing the transfer of energy and momentum within the atmospheric layers from the surface to the lower thermosphere. Most modern numerical models of the global climate, due to the specifics of the problems being solved, are not able to resolve the atmospheric wave of the meso- and lower-scale on their spatial grid. Therefore, various parametrization schemes for wave effects are developed to take into account the impact of OGW. This study is devoted to a detailed description of the new version of the OGW parametrization created on the basis of solving the wave energy balance equation taking into account the Earth rotation. The new version of the parametrization was implemented into the chemistry-climate model SOCOL3 (SOlar Climate Ozone Links version 3) and numerical experiments were carried out using both the previous and the new versions of the parametrization. It is shown, in particular, that the new version of the OGW parametrization allows for more detailed calculation of wave accelerations and heating rates, especially in the lower stratosphere, while the OGWs propagate to greater heights than in the previous parametrization, which better corresponds to observations. As a result, this allows us to obtain more realistic profiles of the mean wind and temperature calculated by the model SOCOL3 with the new parametrization, and the possibilities for fine-tuning the new parametrization provide a significant expansion of a range of scenarios for numerical experiments.

Keywords: Orographic gravity waves, mesoscale atmospheric waves, subgrid-scale orography, wave drag, wave heating rates, atmospheric circulation.

Citation: Koval A. V., Gavrilov N. M., Zubov V. A., Rozanov E. V., and Fadeev A. S. (2025), A New Version of Parametrization of Orographic Waves: Dynamic and Thermal Effects in the SOCOL3 Model, *Russian Journal of Earth Sciences*, 25, ES5014, EDN: UGIGPG, https://doi.org/10.2205/2025es001027

Research Article

Received: January 27, 2025
Accepted: June 10, 2025
Published: October 17, 2025

1. Introduction

Orographic gravity waves (OGWs) serve as a key mechanism coupling the free atmosphere with the Earth's surface, facilitating the transfer of energy and momentum. Consequently, they influence the dynamics and circulation of all atmospheric layers – from the surface to the lower thermosphere [*Fritts et al.*, 2018; *Gavrilov et al.*, 2015, 2018; *Kaifler et al.*, 2015; *Koval et al.*, 2019a]. OGWs belong to the class of internal gravity waves (IGWs), with their most powerful and persistent source being the interaction between atmospheric motions and terrain irregularities [*Durran*, 1990; *Gavrilov et al.*, 2013, 2015; *Koval et al.*, 2024; *Lilly and Kennedy*, 1973; *Smith et al.*, 2008]. In recent years, several major international projects (e.g., DEEPWAVE [*Fritts et al.*, 2018]; COORDE [*Niekerk et al.*, 2018, 2020]) have focused on studying OGW effects across atmospheric layers. The DEEPWAVE project investigated OGW propagation using remote sensing instruments aboard the Gulfstream V and DLR Falcon research aircraft, complemented by ground-based measurements on New Zealand's South Island and Tasmania. The COORDE initiative aimed to unite the scientific community to share methodologies for OGW impact calculations and minimize discrepancies in OGW effects across numerical models.

Most modern global climate models lack the spatiotemporal resolution to explicitly resolve meso-scale and small-scale atmospheric waves, including OGWs. Thus, various parametrization schemes have been developed to account for OGW effects. These effects manifest as mean-flow acceleration and heat fluxes generated by wave dissipation – key outputs calculated in current OGW parametrizations. Wave-induced acceleration of the mean horizontal wind and heat fluxes intensifies during winter [*Gavrilov et al.*, 2013; *Hoffmann et al.*, 2013], when eastward-directed winds at all altitudes (surface to lower thermosphere) promote vertical OGW propagation.

To date, multiple OGW parametrizations have been proposed. A widely used example is the subgrid-scale orography parametrization by *Lott and Miller* [1997], where OGW amplitude is vertically constrained by instability assessed via the critical Richardson number. In this scheme, wave accelerations are derived as the vertical derivative of the wave momentum flux, occurring when waves reach critical levels or become unstable and break. Similar principles underpin other parametrizations [*Iwasaki et al.*, 1989; *McFarlene*, 1987; *Scinocca and McFarlane*, 2000; *Webster et al.*, 2003]. Some schemes additionally incorporate resonance and wave reflection effects alongside dissipation [*Catry et al.*, 2008; *Geleyn et al.*, 1994; *Zhao et al.*, 2018].

This study presents a detailed description of a new OGW parametrization, whose key distinction from existing approaches lies in solving the energy balance equation while accounting for planetary rotation. After implementing the new scheme in the SOCOL version 3 chemistry-climate model (SOlar Climate Ozone Links version 3, [*Stenke et al.*, 2013]), we conducted numerical experiments to compare the updated parametrization with the model's original scheme and to optimize its performance.

2. Description of the OGW Parametrization

The new version of the parametrization described here represents an upgrade to the numerical scheme for OGW effects developed by *Gavrilov and Koval* [2013]. The key modifications in this version include: a new formula for calculating OGW-induced heat fluxes, optimization of the computational code to improve the parametrization's performance, implementation of updated, more realistic vertical profiles of molecular viscosity and thermal conductivity coefficients. These changes are described in detail below.

2.1. Dynamic and Thermal Effects of OGWs

Stationary mesoscale disturbances generated by the interaction of atmospheric flows with Earth's topography belong to the class of internal gravity waves (IGWs) with zero frequencies ($\sigma = 0$). As IGWs propagate – accounting for dissipation and planetary rotation – energy is exchanged between the mean flow and the waves. Under the assumptions of stationarity and horizontal homogeneity of the background fields, the wave-averaged energy balance equation is expressed as follows [*Gavrilov*, 1989]:

$$\frac{\partial F_E}{\partial z} = -\overline{\rho} D - \overline{\rho}\,\overline{v}_\alpha a_{w\alpha}, \tag{1}$$

$$a_{w\alpha} = -\frac{1}{\overline{\rho}}\frac{\partial\left(\overline{\rho}\,\overline{v'_\alpha w'}\right)}{\partial z}, \tag{2}$$

$$F_E = \overline{p'w'} + \overline{\rho v}_\alpha \overline{v'_\alpha w'} - \overline{\left(\sigma'_{z\beta} + \tau'_{z\beta}\right)v'_\beta}, \tag{3}$$

where ρ, p are atmospheric density and pressure; v_β, $v_\beta$and w are velocity components of atmospheric flows along horizontal x_β, x_β and vertical z axes respectively. Summation is performed over repeated Greek indices. In Equations (1)–(3), F_E represents the total wave energy transport, which includes wave energy flux and its transport by atmospheric flow, as well as turbulent and molecular diffusion; D is energy dissipation; $a_{w\alpha}$ is wave acceleration of the mean flow along horizontal axes; $\sigma_{z\beta}$ and $\tau_{z\beta}$ are tensors of molecular and turbulent

viscosity. The overbars denote wave-period averaging, while primes denote wave components of corresponding quantities. The terms on the right-hand side of Equation 1 describe wave energy dissipation and nonlinear interaction between the wave and atmospheric flow.

In *Gavrilov*'s [1989] work, it is discussed that by knowing the vertical gradient of mean wind, one can derive relationships connecting the wave energy dissipation rate and the mean flow acceleration created by the wave. These dependencies form the basis of the current parametrization scheme. For examining the propagation of plane monochromatic wave components, it is convenient to use two horizontal axes ξ and η, directed along the horizontal wave vector k and normal to it, respectively. Let us consider a stationary horizontally-homogeneous model with an altitude-varying mean wind profile. To calculate the wave acceleration component generated by a plane IGW along the ξ axis, we will use the formulas derived by *Gavrilov* [1989]:

$$a_{w\xi} = \frac{k}{\sigma - k\overline{v}_\xi}\left\{D - \frac{1}{\overline{\rho}}\frac{\partial}{\partial z}\left[\overline{\left(\sigma_{z\beta} + \tau_{z\beta}\right)v'_\beta} - \left(\frac{\partial \overline{v}_\xi}{\partial z}\right)^{-1}\overline{\left(\frac{p'}{\overline{\rho}} + v'_\xi\left(\overline{v}_\xi - \frac{\sigma}{k}\right)\right)\frac{\partial\left(\sigma_{\alpha\xi} + \tau_{\alpha\xi}\right)}{\partial x_\alpha}}\right]\right\}. \quad (4)$$

The total heating rate due to the transfer and dissipation of IGW energy is described as follows:

$$\varepsilon_w = D + \overline{v}_\xi a_{w\xi} - \frac{1}{\overline{\rho}}\frac{\partial}{\partial z}\left[\frac{(\gamma-1)\overline{\rho}\,\overline{T}}{gB}\overline{(\varepsilon'_t + \varepsilon'_m + \varepsilon'_r)s'}\right], \quad (5)$$

where $B = (\gamma - 1) + \frac{\partial c_s^2}{g\partial z}$ is the atmospheric static stability parameter; $\gamma = \frac{c_p}{c_v}$ is the heat capacity ratio; T is temperature; g – acceleration dur to gravity; c_s – speed of sound; $\varepsilon t'$, ε'_m, ε'_r are eddy components of heat flux due to turbulent, molecular viscosity, and radiative heat transfer, respectively; $s' = \frac{(p' - c_s^2\rho')}{(\gamma-1)\rho_0 T_0}$ – the eddy entropy component.

The polarization relations for stationary IGWs with zero frequencies $\sigma = 0$ in a rotating atmosphere can be expressed as follows [*Gossard and Hooke*, 1975]:

$$\begin{aligned} &U = -k^2\overline{v}_\xi c_s^2 kX; \quad V = ifkc_s^2 mX; \quad W = \overline{v}_\xi k^3 c_s^2 X; \\ &R = \left[\left(k^2{\overline{v}_\xi}^2 - f^2\right)m + \frac{ik^2c_s^2N^2}{g}\right]X; \\ &P = \gamma c_s\left(k^2{\overline{v}_\xi}^2 - f^2\right)mX; \\ &\Theta = \left[(\gamma-1)\left(k^2{\overline{v}_\xi}^2 - f^2\right)m - \frac{ik^2c_s^2N^2}{g}\right]X, \end{aligned} \quad (6)$$

where U, V, W – amplitude variations of velocity components along η and z axes; R, P, Θ – amplitude variations of density, pressure and temperature; X is an arbitrary constant; f is the Coriolis parameter; m – vertical wavenumber; N – Brunt–Väisälä frequency.

The solution to the system of Equations (6) for amplitude variations of corresponding parameters can be expressed as:

$$\frac{u'}{U_{\max}} = \frac{v'}{U_{\min}} = \frac{w'}{W} = \frac{p'}{p_0 P} = \frac{\rho'}{\rho_0 R} = \frac{T}{T_0\Theta} = e^{\alpha z}. \quad (7)$$

Here, $\alpha = 1/(2H)$, where H is the pressure scale height; u, v, w are the wind components along the horizontal and vertical axes. Taking into account the condition for orographic gravity waves (OGWs) regarding the horizontal wavenumber $|k| >> \frac{f}{|\overline{v}_\xi|}$, which holds true for most OGWs, we can compare the first two relations in (6). The amplitude of velocity oscillations V along the η-axis (perpendicular to the horizontal wave vector k) is typically negligible compared to the amplitude U along the ξ-axis, which is directed parallel to the wave vector. Therefore, in the following analysis, we will consider only the amplitude of the velocity component U. From the dispersion equation, which generally

relates the wave frequency to the horizontal and vertical wavenumbers, we obtain for the case of stationary waves with frequencies $\sigma = 0$:

$$m^2 = \frac{N^2}{\overline{v}_\xi{}^2}\left(1 - \frac{f^2}{k^2\overline{v}_\xi{}^2}\right)^{-1}. \tag{8}$$

Using Equations (1–5), we obtain expressions for the total energy transport by OGWs, wave acceleration along the ξ axis, and the total heating generated by stationary waves. In deriving these formulas, we also employ the polarization relations (6), the dispersion Equation 8, and the relations for $\sigma_{\alpha\beta}$, $\varepsilon_t + \varepsilon_m$ and ε_r presented in the work of *Gavrilov and Popov* [2022]. By utilizing Equations (4) and (5), we can derive expressions for the dissipation D and formulas for the total wave energy transport, wave acceleration, and heat flux:

$$\begin{aligned} F_E &= -\frac{\overline{\rho} f^2 U^2}{2mk\overline{v}_\xi}, \\ a_{w\xi} &= -\frac{k^2U^2}{\left(2\overline{v}_\xi\right)}(\nu_z + \kappa_z)\left(1 + \frac{1}{(\gamma-1)\,\mathrm{Pr}}\right), \\ \varepsilon_w &= \frac{1}{\rho}\left(\delta(\nu_z Z) + \frac{\gamma H}{2(\gamma-1)}\frac{d}{dz}(\kappa_z Z)\right), \quad \delta = \frac{f^2}{k^2}\frac{\partial}{\partial z}\left(\frac{\partial \overline{v}_\xi^2}{\partial z}\right)^{-1}, \end{aligned} \tag{9}$$

where δ – a parameter depending on the vertical shear of horizontal wind; $\nu_z = \nu + K_z$ and $\kappa_z = \kappa + K_{zt}$, where ν, K_z, κ, K_{zt} are the coefficients of molecular and turbulent viscosity and thermal conductivity, respectively; $Z = \overline{\rho} m^2 U^2$; Pr – the effective Prandtl number. The kinematic coefficients of molecular viscosity ν and thermal conductivity κ are calculated using Sutherland's formula [*Tables...*, 1976]:

$$\nu = \frac{1.46 \times 10^{-6}\sqrt{T_0}}{\rho\left(1 + \frac{110}{T_0}\right)}; \quad \kappa = \frac{\nu(9\gamma - 5)}{4\gamma}. \tag{10}$$

The background vertical profiles of turbulent viscosity feature maxima of $10\,\mathrm{m^2\,s^{-1}}$ near the Earth's surface and at 100 km altitude, with a minimum of $0.1\,\mathrm{m^2\,s^{-1}}$ in the stratosphere [*Gavrilov and Kshevetskii*, 2014]. It should be noted that when $\delta = 1$, the expression for ε_w in (9) represents the wave energy dissipation rate due to molecular and turbulent viscosity and thermal conductivity, which is widely used to estimate the thermal effect of stationary mesoscale waves. In the first version of the OGW parametrization [*Gavrilov et al.*, 2013, 2015], the value $\delta = 1$ was used in (9). To obtain an equation describing the variation of velocity oscillation amplitude U with height, we use Equation 1 and the first equation in (9), which leads to

$$\frac{\partial}{\partial z}\left(\frac{\overline{\rho} f^2 U^2}{|k|N}\sqrt{1 - \frac{f^2}{k^2\overline{v}_\xi{}^2}}\right) = -2\overline{\rho}(\nu + K_z)\delta m^2 U^2. \tag{11}$$

From Equation 9 for ε_w and Equation 11, it can be shown that the divergence of the upward total energy flux of OGWs is proportional to $-\varepsilon_w$. Therefore, when $\delta > 0$, wave energy dissipation leads to atmospheric heating $\varepsilon_w > 0$, which represents the typical situation. This also corresponds to a decrease in the total wave energy flux with altitude. However, under certain vertical wind shears, δ can become negative when the second vertical derivative of $\overline{v}_\xi^2$ is negative. This corresponds to local atmospheric cooling by OGWs ($\varepsilon_w < 0$) and an increase in the total wave energy flux with altitude.

The convective stability condition for OGWs takes the form $\partial\overline{T}/\partial z + \partial T'/\partial z + \gamma_\alpha > 0$, where T' represents temperature variations and a $\gamma_a = g/c_p$ is the adiabatic temperature gradient. For stationary OGWs with zero horizontal phase velocity, this condition is equiv-

alent to $U < |\overline{v}_\xi|$. In our OGW parametrization, we locally enforce $U = |\overline{v}_\xi|$ in regions of wave instability (when $U > |\overline{v}_\xi|$). Our test calculations with the new OGW parametrization, using specified background wind and temperature profiles [*Koval et al.*, 2024], demonstrated that the implemented changes in viscosity and thermal conductivity profiles, along with accounting for background wind shears through parameter δ, enabled more detailed calculation of OGW parameters and yielded good agreement between the resulting wave acceleration profiles and those obtained in the OGW parametrization intercomparison projects COORDE [*Niekerk et al.*, 2020] and CMIP6 (see the parametrization review in [*Hájková and Šácha*, 2023]).

Equations (9) exhibit singularities when $|\overline{v}_\xi| \to f/|k|$, $|\overline{v}_\xi| \to 0$ and $\partial|\overline{v}_\xi|/\partial z \to 0$. The first case corresponds to a critical level where $m^2 \to \infty$ in Equation 9, implying strong dissipation of short OGWs. The second case occurs near the level where the horizontal wind becomes perpendicular to the OGW propagation direction ξ, causing $|\overline{v}_\xi| \to 0$. We assume that OGWs completely dissipate in this region, and set $U = 0$ above the critical level. At altitudes where $\partial|\overline{v}_\xi|/\partial z \to 0$

Given the wave amplitude U at the lower boundary and vertical profiles of $\overline{v}_\xi$ and $\overline{T}$, Equation 11 can be solved for the square of the OGW amplitude, U^2. A finite-difference grid is used for the vertical coordinate with step size Δz. The recurrence relation connecting U^2_{i+1} and U^2_i at the $(i+1)$-th and i-th nodes of the vertical grid has the following form:

$$\begin{gathered} U^2_{i+1} = \frac{r_i}{r_{i+1}} U^2_i \exp\left[-\frac{s_i}{r_i}\Delta z\right], \\ r_i = \frac{\overline{\rho}_i f^2}{2|k|N_i}\sqrt{1 - \frac{f^2}{k^2\overline{v}^2_\xi}}, \quad s_i = \overline{\rho}_i(\nu_i + K_{zi}){m_i}^2\delta_i, \end{gathered} \tag{12}$$

where the index i denotes values at altitude level $z = z_i$. To sequentially solve Equation 12 at each level starting from the bottom, we require a lower boundary condition for U^2. To obtain this, we use the subgrid-scale orography parametrization described below.

2.2. Subgrid-Scale Surface Topography Parametrization

For parametrizing Earth's surface height inhomogeneities, we employ a modification of the method proposed by *Baines and Palmer* [1990] and later used by *Lott and Miller* [1997]. This approach utilizes the concept of "subgrid-scale" orography, meaning accounting for land surface relief with horizontal scales smaller than the horizontal grid spacing of the numerical model. At each grid point, an elliptical approximation of subgrid-scale topography is used [*Lott and Miller*, 1997]:

$$h(x', y') = \frac{h_m}{1 + \left(\frac{x'}{a}\right)^2 + \left(\frac{y'}{b}\right)^2}, \tag{13}$$

where h_m is the effective height of the topographic irregularity, a and b are the minor and major semi-axes of the ellipse, and x' and y' are the coordinate axes oriented along these semi-axes respectively (see Figure 1).

The forces acting on an elliptical barrier by horizontal flow have been investigated in [*Scinocca and McFarlane*, 2000]. In accordance with Newton's 3rd law, the mountain barrier exerts an equal and opposite force on the atmosphere. This force is equivalent to the vertical flux of horizontal momentum $\vec{F}_m$ generated by OGWs. The components of this flux per unit area – the along-flow component F_{mv}, and cross-flow component F_{mn}, – are described by the following expressions [*Baines and Palmer*, 1990]:

$$\begin{aligned} F_{mv} &= \rho_0 v_0 N_0 \mu\sigma G\left(B\cos^2\chi + C\sin^2\chi\right), \\ F_{mn} &= \rho_0 v_0 N_0 \mu\sigma G(B - C)\sin\chi\cos\chi, \end{aligned} \tag{14}$$

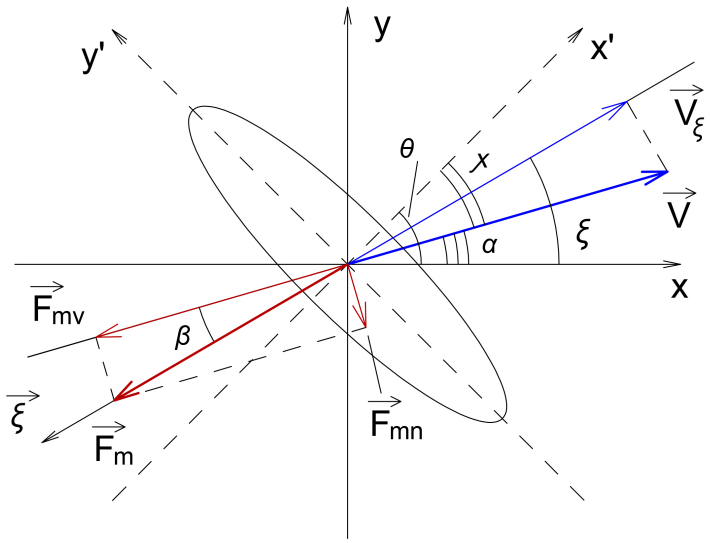

Figure 1. Schematic orientation of an elliptical mountain barrier in the horizontal plane. The x- and y-axes point eastward and northward, respectively; the x'- and y'-axes represent the minor and major axes of the elliptical mountain ridge; the ξ-axis indicates the propagation direction of OGWs and wave acceleration. Blue vectors show the surface wind direction and its projection onto the ξ-axis. Red arrows indicate the components of forces exerted by the mountain ridge on the atmosphere.

where the subscript 0 denotes values at the lower boundary for Equation 11, which uses the first node of the model's vertical grid located above the mean Earth surface height at each grid point; v_0 is the mean horizontal wind velocity at this level, directed at angle α to the x-axis; $\mu = \sqrt{\left(\overline{h} - h\right)^2}$ is the standard deviation of Earth surface height variations; χ is the angle between wind direction and the minor axis of the elliptical barrier ($\chi = \theta - \alpha$, see Figure 1); σ is the slope parameter, G is the mountain sharpness parameter. For the elliptical profile (13), $G = 1.23$ was proposed [*Lott and Miller*, 1997]. The coefficients B and C in (14) are calculated by the formulas: $B = 1 - 0.18\zeta - 0.04\zeta^2$, $C = 0.48\zeta + 0.3\zeta^2$, where ζ is the parameter characterizing subgrid-scale topography anisotropy. In the formula for μ, the overbar denotes averaging over a selected horizontal area centered at the given point.

The components (F_{mv}, F_{mn}), calculated at the model's lower level, determine the OGW propagation direction and consequently the mean flow acceleration due to OGWs along the ξ-axis, oriented at angle β relative to the horizontal wind direction, as shown in Figure 1. The angle between the OGW acceleration vector and the zonal x-axis is $\xi = \alpha + \beta$. To determine the geometric parameters of subgrid topography σ and ζ (the slope parameter and subgrid topography anisotropy, respectively), we refer to the topographic gradient correlation tensor with the following components [*Zadra et al.*, 2003]:

$$H_{xx} = \overline{\left(\frac{\partial h}{\partial x}\right)^2}, \quad H_{yy} = \overline{\left(\frac{\partial h}{\partial y}\right)^2}, \quad H_{xy} = \overline{\frac{\partial h}{\partial x}\frac{\partial h}{\partial y}}. \tag{15}$$

The angle between the latitudinal circle and the minor axis of the elliptical mountain barrier (denoted as θ in Figure 1) determines the direction of the steepest topographic gradients: "across" the mountain ridge aligned with the ellipse's major axis. This angle is calculated using Equations (15) as follows:

$$\theta = \arctan\left(\frac{2H_{xy}}{H_{xx} - H_{yy}}\right). \tag{16}$$

It is important to note that Equation 16 omits the 1/2 coefficient proposed by *Baines and Palmer* [1990], following the recommendation of *Scinocca and McFarlane* [2000], meaning

the angle between eastward direction and the minor axis of the elliptical mountain barrier varies within $[-\pi/2, \pi/2]$.

The subgrid-scale topography anisotropy ζ reflects the eccentricity of the elliptical barrier:

$$\zeta^2 = \overline{\left(\frac{\partial h}{\partial y'}\right)^2 \left(\frac{\partial h}{\partial x'}\right)^{-2}} = \frac{H_{xx} + H_{yy} - \sqrt{\left(H_{xx} - H_{yy}\right)^2 + 4H_{xy}{}^2}}{H_{xx} + H_{yy} + \sqrt{\left(H_{xx} - H_{yy}\right)^2 + 4H_{xy}{}^2}}. \quad (17)$$

The x' and y' axes in Figure 1 indicate directions along the axes of the elliptical barrier. The slope parameter σ determines the maximum topographic height in the direction transverse to the mountain ridge. Following [*Lott and Miller*, 1997], we use the expression:

$$\sigma^2 = \overline{\left(\frac{\partial h}{\partial x'}\right)^2} = \frac{1}{2}\left(H_{xx} + H_{yy} + \sqrt{\left(H_{xx} - H_{yy}\right)^2 + 4H_{xy}{}^2}\right). \quad (18)$$

For the vertical flux of horizontal momentum in the case of a plane atmosphere accounting for planetary rotation, the following equation is used [*Gossard and Hooke*, 1975]:

$$F_m = \frac{1}{2}\rho_0 v_0 N_0 k_e \mu^2 \cos\theta, \quad (19)$$

where k_e is the effective horizontal wavenumber. By equating Equations (14) and (19) for the components of wave momentum flux, we obtain the effective horizontal wavenumber of OGWs:

$$k = k_e = \frac{2s\sqrt{F_{mv}^2 + F_{mn}^2}}{\rho_0 v_0 N_0 \mu^2 \cos\theta}. \quad (20)$$

Using the polarization relations (6, 7), the wave momentum flux is expressed as follows:

$$F_m = \rho_0 \overline{v'_\xi w'} = \rho_0 U_0{}^2 \frac{\sqrt{k^2 \overline{v}_{\xi 0}^2 - f^2}}{2N_0}. \quad (21)$$

After equaling the right-hand sides of Equations (14) and (21), taking into account (10), (17)–(20), we determine the effective amplitude of OGWs at the lower boundary U_0 of the parametrization. When implementing the parametrization in the SOCOL3 model, the first level above the planetary surface is set as the lower boundary at each horizontal grid point. The values of k and U_0 calculated from Equations (20) and (21) are used as boundary conditions for computing the OGW amplitude U using Equation 12 at all vertical grid points. The projection of mean wind onto the wave direction $\overline{v}_\xi$ in Equations (9) and (11) is obtained as the sum of projections of mean zonal and meridional winds onto the wave momentum flux direction calculated from Equation 14.

3. General Circulation and Climate Modeling

The SOCOL Model. The new version of the OGW effects parametrization described above has been implemented in the chemistry-climate model SOCOL (SOlar Climate Ozone Links) version 3 (SOCOL3). This model combines the ECHAM general circulation model with a modified version of the MEZON chemistry-transport model [*Egorova et al.*, 2003; *Schraner et al.*, 2008]. ECHAM and MEZON are interactively coupled through the exchange of three-dimensional temperature and wind fields from ECHAM to MEZON, along with the transfer of radiatively active water vapor, ozone, methane, and other species in the opposite direction. SOCOL3 features 40 vertical grid levels spanning pressure levels from the Earth's surface to 0.01 hPa (~80 km) and can operate at two horizontal resolutions (T31 and T42). The model's performance has been successfully validated through international model intercomparison projects such as CCMI-1 [*Hegglin et al.*, 2015]. A comprehensive description of SOCOL3 is provided in [*Stenke et al.*, 2013]. The version used in this study (T42) has a horizontal resolution of 64×128 grid points along latitude and longitude,

respectively. Consequently, its resolution is insufficient to explicitly resolve mesoscale waves, necessitating the use of parametrization schemes to account for IGW effects.

The previous subgrid-scale OGW parametrization implemented in SOCOL3, hereafter referred to as LM (*Lott and Miller* [1997]), employs a topographic approximation method similar to that used in the new parametrization. It calculates the momentum transfer from the Earth to the atmosphere generated by OGWs. The primary difference between the LM and new parametrizations lies in the higher latitudinal-longitudinal resolution (2′×2′) of the new scheme, based on ETOPO2 data [*NOAA National Geophysical Data Center*, 2006], compared to the coarser resolution (10′×10′) of the previous version.

As discussed in the Introduction, the LM parametrization assumes that the horizontal momentum flux of OGWs remains constant during upward propagation from the surface, with wave-induced acceleration being zero except when waves reach critical levels and either break or dissipate. The breakdown of OGWs is determined using a criterion based on the critical Richardson number (*Ri*). Notably, multiple critical levels may be encountered during OGW propagation [*Roeckner et al.*, 2003].

The primary difference of the new parametrization, as with its first version [*Gavrilov and Koval*, 2013], lies in calculating vertical profiles of OGW characteristics, wave-induced acceleration, and heat fluxes using Equations (9) and (11) at every horizontal grid point of the SOCOL3 model. Explicit computation of heat fluxes and accelerations at each grid node yields a more detailed spatial structure of these parameters. Crucially, the new scheme accounts for both OGW heating and cooling rates evaluated via Equation 9. When critical levels are reached (where the horizontal wind projection $\overline{v}_\xi \to 0$, indicating wind rotation perpendicular to OGW propagation – see subsection 4.1), OGWs dissipate, with no wave effects above this level.

Residual Meridional Circulation (RMC). OGWs profoundly influence the Brewer-Dobson circulation in the stratosphere [*Butchart*, 2014]. Under the Transformed Eulerian Mean framework, RMC combines Eulerian-mean circulation and the planetary wave (PW) driving term [*Andrews et al.*, 1987]. RMC analysis provides a robust method for studying PW-mean flow interactions, with its formulation comprehensively discussed in [*Koval et al.*, 2021].

Eliassen-Palm (EP) Flux. OGW-induced acceleration (drag) decelerates zonal wind, potentially altering the refractive index for PWs [*Alexander et al.*, 2010]. For instance, 3D nonlinear MUAM simulations demonstrate that OGW forcing can modify PW amplitudes by >50% under specific conditions [*Gavrilov et al.*, 2015], consistent with SOCOL3 experiments [*Koval et al.*, 2024]. To interpret the interaction between PWs and the mean flow and to demonstrate the characteristics of their propagation under different OGW influences, Eliassen-Palm (EP) fluxes were calculated using standard formulations [*Jucker*, 2021]. Here, EP flux represents wave-driven momentum/heat transport, and its divergence reflects PW-induced acceleration of atmospheric circulation flows.

Meridional Heat Flux $\overline{v'T'}$ **(**primes denote deviations from zonal-mean; overbars indicate averaging). Poleward heat flux in linear wave theory reflects upward group velocity of PWs [*Andrews et al.*, 1987]. For detailed analysis of winter troposphere-stratosphere heat flux responses to external forcings, see [*Dunn-Sigouin and Shaw*, 2020].

4. Results

The parametrization described in section 2 underwent testing prior to its implementation in the global circulation model. Vertical profiles of various OGW parameters were examined, along with their relationship to background wind and temperature fields and planetary surface topography features. These results are presented in [*Koval et al.*, 2024]. Following this, the tuned and calibrated parametrization was integrated into the SOCOL3 model, where further fine-tuning was performed.

To validate the functionality of the new OGW parametrization in SOCOL3, numerical simulations of global atmospheric circulation were conducted for January 2016 – a period characterized by relatively quiescent dynamical conditions without sudden stratospheric warming events. Comparative simulations were performed using both the LM parametrization and the new scheme, analyzing multiple atmospheric parameters including temperature, zonal wind, RMC components, heat fluxes, EP fluxes, parametrization-derived wave acceleration and heating rates.

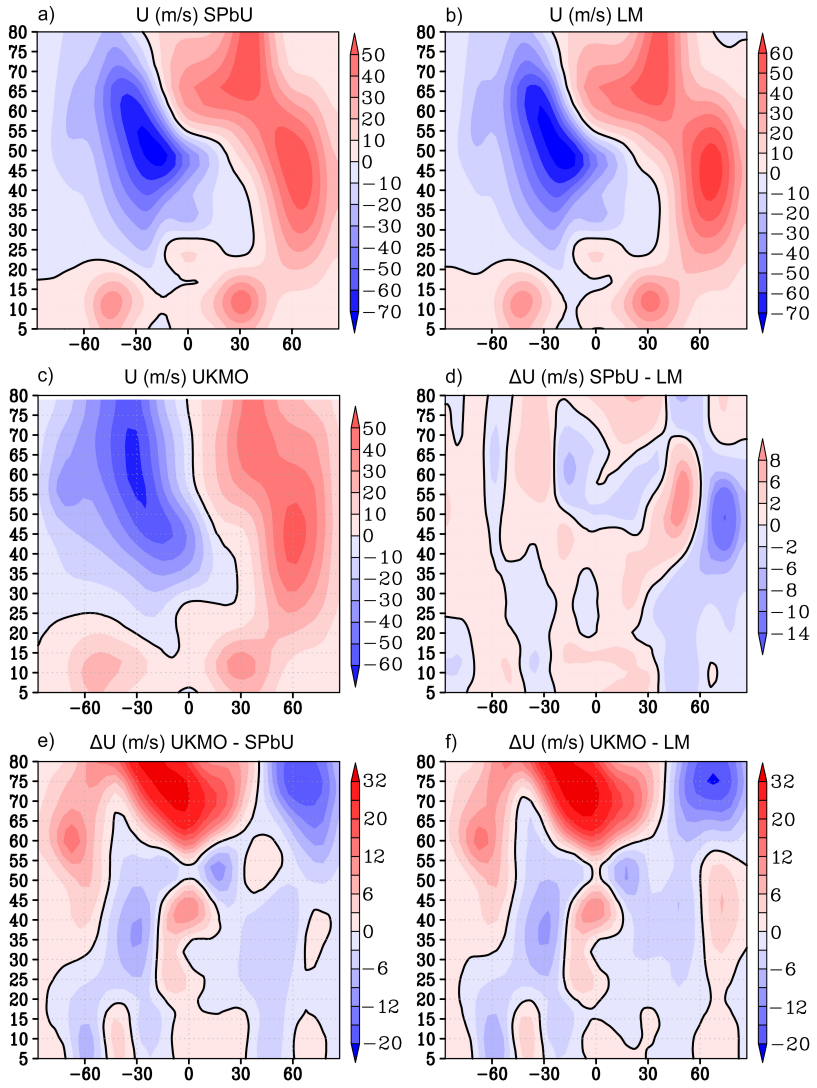

Figure 2. Latitude-altitude distributions of the zonal-mean zonal wind from SOCOL3 simulations with: (a) the new (SPbU) OGW parametrization; (b) the previous (LM) OGW parametrization; (c) corresponding UKMO reanalysis data; (d) differences between the new and previous OGW parametrizations; (e,f) differences between model simulations (a,b) and UKMO reanalysis, respectively.

4.1. Changes in dynamic characteristics

Figures 2a and 2b show latitude-altitude distributions of the zonal-mean zonal wind from simulations with the previous and new OGW parametrizations, respectively. Figure 2c presents the wind distribution from UKMO reanalysis data [*Swinbank and O'Neill*, 1994] for January 2016 for comparison. In the Northern Hemisphere, the zonal wind at all altitudes is eastward (positive), thus creating conditions favorable for planetary wave propagation [*Charney and Drazin*, 1961]. In the troposphere and lower stratosphere, jet streams with

maxima at mid-latitudes form, directed eastward in both hemispheres. In the Southern Hemisphere, in the stratosphere and mesosphere, the zonal wind is directed westward. In the equatorial stratosphere, the observed differences between the reanalysis and modeling data can be associated with changes in the QBO phase.

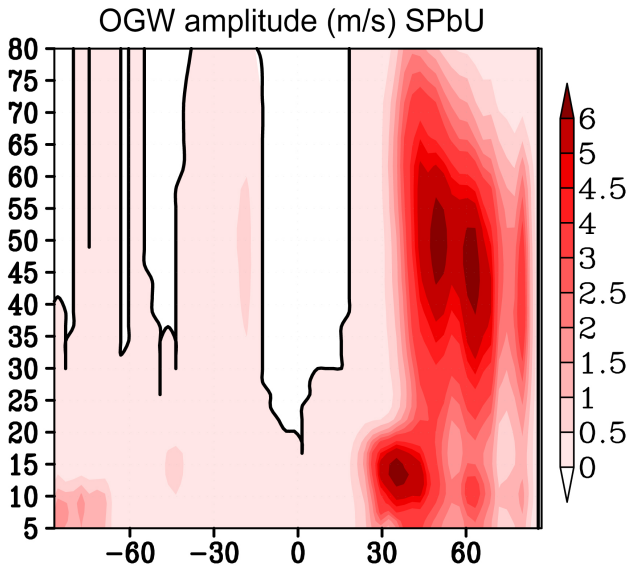

Figure 3. Latitude-altitude distribution of OGW amplitude calculated using the new parametrization.

Figure 3 shows the OGW amplitude calculated with the new parametrization for January. The structure of the stratospheric-mesospheric zonal circulation determines the characteristics of OGW propagation from the troposphere upward. According to Equation 8, as discussed above, the vertical wavenumber $m^2 \to \infty$, when the horizontal wind becomes perpendicular to the wave propagation direction ξ; such short waves dissipate due to turbulent viscosity and thermal conductivity near the critical level at $\overline{v}_\xi \to 0$. These conditions are uncharacteristic for the Northern Hemisphere during winter when winds at all altitudes are eastward, allowing OGWs to propagate up to lower mesosphere altitudes (see Figure 3). In the Southern (summer) Hemisphere, OGWs are filtered at altitudes of approximately 20 km, in layers where horizontal wind reversal occurs, as shown in Figure 2a–c. In addition to the aforementioned reasons for vertical changes in OGW structure, there exists another factor related to Earth's rotation, which is accounted for in Equations (8), (9), and (11). These equations incorporate the Coriolis parameter f, which increases toward high latitudes. This increase in f may facilitate preferential OGW propagation in the middle atmosphere at high latitudes. Detailed descriptions of OGW penetration from tropospheric sources are provided in [*Koval et al.*, 2024].

Figure 2a clearly demonstrates that simulations using the new parametrization show weaker zonal jet streams in the northern stratosphere compared to simulations with the previous parametrization (Figure 2b), better matching reanalysis data shown in Figure 2c. Figures 2d–e display differences between modeled zonal winds (Figure 2a–b) and reanalysis data (Figure 2c). The maximum discrepancies occur in the mesosphere, which relates to model performance and falls outside this study's scope, as OGWs do not propagate into low-latitude mesosphere (Figure 3 and 4). In the northern stratosphere, the new parametrization reduces discrepancies between modeled zonal winds and reanalysis at all altitudes (Figure 2d) compared to the LM parametrization (Figure 2e). Figure 2g presents differences in zonal winds simulated in SOCOL with different OGW parametrizations. The northern stratosphere above 30°N shows maximum differences, with their spatial distribution corresponding to OGW propagation trajectories in the Northern Hemisphere (amplitudes shown in Figure 3). Our subsequent analysis will focus specifically on the Northern Hemisphere.

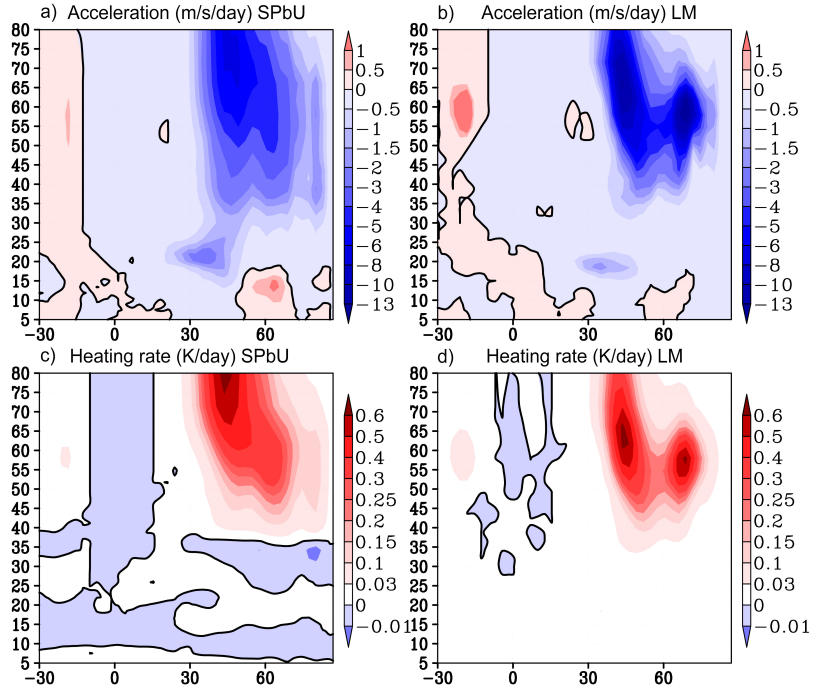

Figure 4. Distributions of OGW wave accelerations (a, b) and heating rates (c, d) from SOCOL3 model simulations using the new (left) and previous (right) OGW parametrizations, respectively. The latitudinal range spans from 30°S to 90°N.

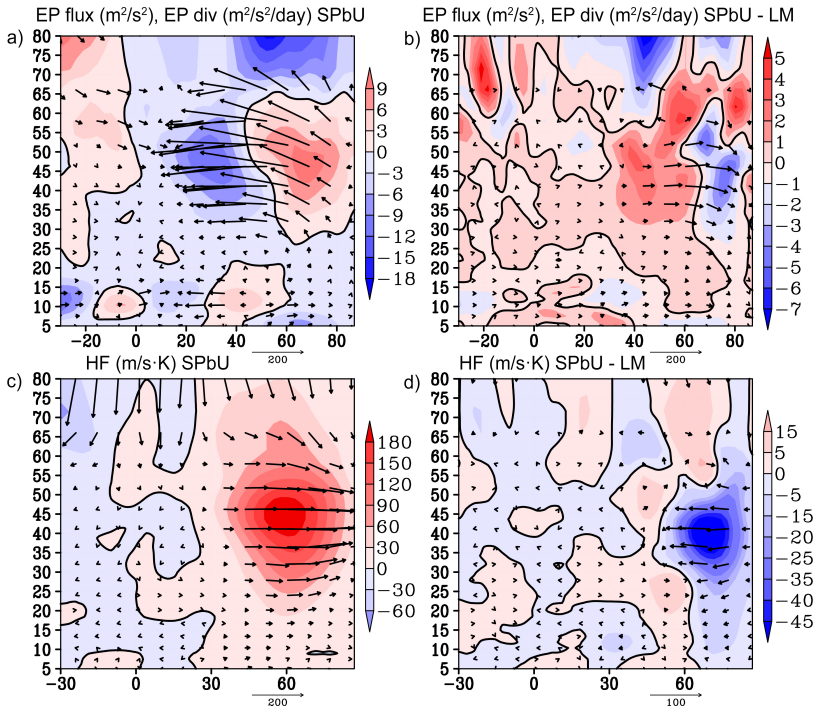

Figure 5. EP flux divergence (color shading) and its meridional components (arrows) (a); meridional wave heat flux (color shading) and its meridional components (arrows) (c) from SOCOL3 simulations with the new OGW parametrization; (b, d) show differences between corresponding quantities calculated with new and previous parametrizations.

Figures 4a and 4b display OGW accelerations calculated using the new and previous parametrizations, respectively. As discussed above and according to Equation 9, these accelerations oppose the incoming wind flow (at angle β, see Figure 1). Peak acceleration

values occur above 50–60 km, with smaller magnitudes in the new parametrization (Figure 4a) compared to the previous one. The region of non-zero values is larger in the new parametrization, and the acceleration structure in the lower stratosphere (10–30 km) shows finer detail in Figure 4a compared to Figure 4b.

Let us examine the effects of different OGW parametrizations from the perspective of wave-mean flow interactions. Figure 5a shows EP flux divergence and its meridional components (arrows), while Figure 5b displays changes induced by different OGW parametrizations (new one minus previous). Wave activity propagates along waveguides in the Northern Hemisphere [*Koval et al.*, 2022, 2019b], with EP flux arrows pointing upward and equatorward in Figure 5a. Positive EP flux divergence in the polar stratosphere (above 50°N) corresponds to reduced wave activity and momentum transfer to the mean flow, thereby accelerating zonal winds. However, when using the new parametrization, Figure 5b shows reduced EP flux divergence in the polar stratosphere compared to the previous scheme, leading to weaker momentum transfer and consequently weaker zonal winds (as seen in Figure 2d). The 40°–60°N region in Figure 2d and 5b shows opposite trends, with mean flow acceleration and enhanced EP flux divergence.

Changes in wave activity can also be demonstrated through modifications in wave heat fluxes (Figure 5c for new parametrization and 5d for differences). Poleward-directed meridional heat fluxes correspond to upward-propagating wave activity and polar stratospheric heating. However, the new parametrization reduces these stratospheric fluxes, consequently decreasing polar heating as discussed in the following subsection.

4.2. Thermal Structure

Figures 6a and 6b present latitude-altitude distributions of zonal-mean temperature from simulations using the new and previous OGW parametrizations, respectively, with arrows indicating RMC velocity vectors. The temperature distributions are characteristic of the winter season in the Northern Hemisphere: in the troposphere, temperatures at the equator are predictably higher than at the poles; the winter polar stratosphere, where the stratospheric polar vortex forms, exhibits a local temperature minimum; above this, temperatures increase up to the stratopause, with the summer polar stratopause being warmer due to solar heating during polar day; above 50 km, temperatures decrease, forming a temperature minimum in the summer mesopause (near 80 km), which owes its existence to enhanced upward motions in this region as part of the global meridional circulation, indicated by the arrows.

For comparison with model results, an analogous temperature distribution was constructed using UKMO reanalysis data (Figure 6c). The temperature difference between the two parametrizations is shown in Figure 6d. The polar region between 40–65 km shows lower temperatures with the new parametrization. This temperature change results not only from reduced direct heat fluxes in the new parametrization during OGW dissipation compared to the previous scheme (Figure 4c and 4d, respectively), but also from dynamic effects: as shown in the previous subsection, planetary wave activity weakens in the 25–60 km polar region. This reduces the wave-driven contribution to RMC, explaining why RMC increment arrows in the cooling region of Figure 6d point upward – indicating weakened descending RMC branches and consequently reduced adiabatic heating in polar regions. For additional comparison of parametrizations, Figures 3e–f show temperature differences between model calculations and reanalysis. It can be observed that the contribution of OGW parametrization to the temperature field is relatively small compared to temperature changes in the mesosphere, where the model overestimates temperatures. In the northern polar stratosphere, the model with the previous parametrization (Figure 6e) shows stronger temperature overestimation above 45 km and underestimation in the 20–30 km layer, while with the new parametrization the temperature in this region better matches reanalysis data. This improvement is also evident in the 40°–70°N latitude band, where temperatures with the new parametrization are lower than with the previous one.

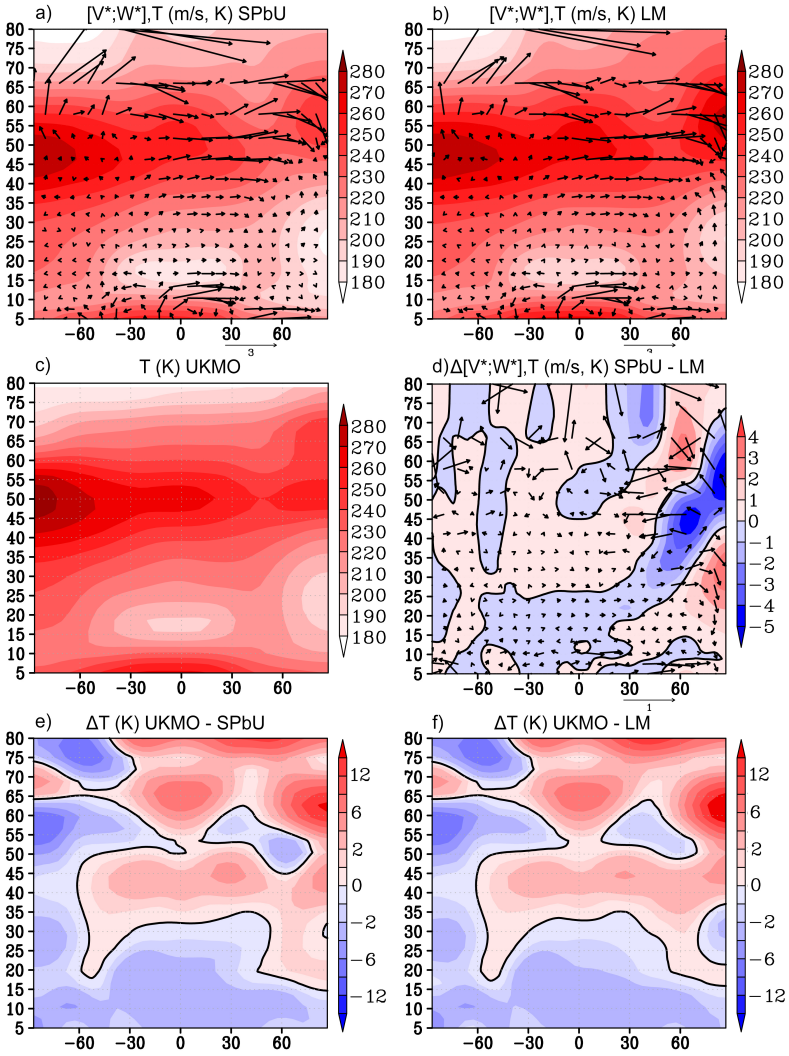

Figure 6. Latitude-altitude distributions of zonal-mean temperature (color shading) and RMC components (arrows) from SOCOL3 simulations with (a) new and (b) previous OGW parametrizations; (c) corresponding UKMO reanalysis temperature distribution. Differences in temperature and RMC between new and previous OGW parametrizations (d); temperature differences between model simulations (a, b) and UKMO reanalysis (e, f respectively).

Detailed examination of OGW heat fluxes in Figure 4c–d reveals that while peak values are smaller with the new parametrization, it provides more refined calculations. Notably, the new scheme produces localized cooling in the northern stratosphere (25–35 km) associated with zonal wind structure creating negative second height derivatives in Equation 9's δ parameter. Importantly, the new parametrization allows OGWs to propagate to greater altitudes, potentially influencing thermospheric processes in comprehensive models, as significant OGW effects are observed up to lower thermosphere heights [*Gavrilov et al.*, 2015, 2018; *Koval et al.*, 2019a]. This extended vertical propagation is corroborated by numerous observational studies [*Fritts et al.*, 2018, 2019; *Heale et al.*, 2020; *Smith et al.*, 2009].

Overall analysis of SOCOL simulations with different OGW parametrizations demonstrates that: (1) OGWs substantially impact atmospheric modeling, and (2) the new parametrization improves circulation representation. The new scheme enables more precise atmospheric process modeling, offering potential for further refinements, though initial experiments already show marked improvements over the previous parametrization.

5. Conclusion

This study presents a detailed description of the new version of the parametrization for thermal and dynamic effects of orographic gravity waves (OGWs), developed by *Gavrilov and Koval* [2013], and its implementation in the SOCOL3 chemistry-climate model. The parametrization is based on the wave energy balance equation, deriving formulas for calculating the total vertical wave energy flux and amplitudes of horizontal wind velocity variations induced by OGWs. Using refined polarization relations for stationary IGWs in a rotating atmosphere, Gavrilov and Koval obtained formulas for OGW-induced accelerations and heat fluxes, and developed a subgrid-scale topography parametrization. The new OGW parametrization version contains several substantial modifications compared to the earlier version [*Gavrilov and Koval*, 2013]:

- Calculation of OGW amplitude at the lower boundary U_0 (Equation 21) in SOCOL3 now begins at the first model level above Earth's surface at each grid point, whereas the earlier parametrization fixed boundary conditions at 7 km altitude [*Gavrilov et al.*, 2013, 2015];
- The *theta* parameter (angle between x-axis and elliptical barrier orientation, Equation 16) omits the 1/2 coefficient proposed by *Baines and Palmer* [1990], following *Scinocca and McFarlane*'s [2000] recommendation;
- Implementation of new realistic vertical profiles for molecular viscosity and thermal conductivity coefficients;
- New formula for calculating ε_w, OGW heating rates (9);
- The δ parameter (Equation 9) was set to 1 in the earlier version, reproducing only wave heating (not cooling) effects;
- Code optimization for parallel computing to accelerate parametrization performance.

Test simulations using the new parametrization version with prescribed 3D background wind and temperature fields are described in [*Koval et al.*, 2024], which presents the logic of OGW propagation from sources depending on surface topography, equatorial distance, and background parameter profiles.

Following implementation in SOCOL3, comparative numerical experiments were conducted using both the new parametrization and the previous "Lott and Miller" scheme employed in earlier model versions.

The main results can be summarized as follows:

- The most significant changes in dynamic and temperature parameters between the new and previous parametrizations are predictably observed in the northern stratosphere along OGW propagation trajectories.
- The peak values of OGW-induced accelerations calculated by the new parametrization occur at higher altitudes and are smaller in magnitude compared to the previous parametrization. However, in the lower stratosphere, the new version provides more detailed acceleration structures with a stronger contribution to zonal wind deceleration. Consequently, with the new parametrization, the zonal jet stream in the northern stratosphere is weaker than in simulations using the previous scheme, better matching observational data. This stratospheric jet weakening is also associated with reduced Eliassen-Palm (EP) flux divergence, indicating diminished momentum transfer from planetary waves due to decreased wave activity in polar regions.
- In the northern stratosphere-mesosphere, the model with the new parametrization better reproduces temperature fields, while the previous scheme overestimates temperatures. This temperature change results from both reduced direct heat fluxes during OGW dissipation in the new parametrization and dynamic effects: weakened planetary wave activity in polar regions reduces the wave-driven contribution to RMC, decreasing descending RMC branches and subsequent adiabatic heating in polar areas. Changes in wave activity are also evident in heat fluxes. The poleward-directed meridional heat flux, corresponding to upward-propagating wave activity and polar stratospheric heating, becomes weaker in the new parametrization, contributing to polar region cooling.

Thus, we conclude that the new OGW parametrization version can realistically reproduce OGW effects from the surface to the upper mesosphere and potentially to higher altitudes. Its capacity for fine-tuning enables a wide range of scenario experiments. Future work will focus on implementing this parametrization in other global circulation models like MUAM [*Koval et al.*, 2022, 2019b], conducting numerical studies of OGW impacts on atmospheric dynamics, thermal regimes, and composition across different seasons and climate conditions, including future climate projections.

Acknowledgments: Numerical modeling was performed on the computing cluster of the Laboratory for Ozone Layer and Upper Atmosphere Research with support from St. Petersburg State University (Project ID 124032000025-1). Analysis of global wave interactions, RMC calculations, heat fluxes, and EP fluxes were supported by the Russian Science Foundation grant No. 25-47-00122, https://rscf.ru/project/25-47-00122.

References

Alexander M. J., Geller M., McLandress C., et al. Recent developments in gravity-wave effects in climate models and the global distribution of gravity-wave momentum flux from observations and models // Quarterly Journal of the Royal Meteorological Society. — 2010. — Vol. 136, no. 650. — P. 1103–1124. — https://doi.org/10.1002/qj.637.

Andrews D. G., Holton J. R. and Leovy C. B. Middle atmosphere dynamics. — New York, USA : Academic Press, 1987. — 483 p.

Baines P. G. and Palmer T. N. Rationale for a new physically-based parametrization of subgrid-scale orographic effects // Technical memorandum. — 1990. — No. 169. — https://doi.org/10.21957/H4H36B3U.

Butchart N. The Brewer-Dobson circulation // Reviews of Geophysics. — 2014. — Vol. 52, no. 2. — P. 157–184. — https://doi.org/10.1002/2013rg000448.

Catry B., Geleyn J., Bouyssel F., et al. A new sub-grid scale lift formulation in a mountain drag parameterisation scheme // Meteorologische Zeitschrift. — 2008. — Vol. 17, no. 2. — P. 193–208. — https://doi.org/10.1127/0941-2948/2008/0272.

Charney J. G. and Drazin P. G. Propagation of planetary-scale disturbances from the lower into the upper atmosphere // Journal of Geophysical Research. — 1961. — Vol. 66, no. 1. — P. 83–109. — https://doi.org/10.1029/jz066i001p00083.

Dunn-Sigouin E. and Shaw T. Dynamics of Anomalous Stratospheric Eddy Heat Flux Events in an Idealized Model // Journal of the Atmospheric Sciences. — 2020. — Vol. 77, no. 6. — P. 2187–2202. — https://doi.org/10.1175/jas-d-19-0231.1.

Durran D. R. Mountain Waves and Downslope Winds // Atmospheric Processes over Complex Terrain. — American Meteorological Society, 1990. — P. 59–81. — https://doi.org/10.1007/978-1-935704-25-6_4.

Egorova T. A., Rozanov E. V., Zubov V. A., et al. Model for investigating ozone trends (MEZON) // Izvestiya, Atmospheric and Oceanic Physics. — 2003. — Vol. 39, no. 3. — P. 277–292.

Fritts D. C., Vosper S. B., Williams B. P., et al. Large-Amplitude Mountain Waves in the Mesosphere Accompanying Weak Cross-Mountain Flow During DEEPWAVE Research Flight RF22 // Journal of Geophysical Research: Atmospheres. — 2018. — Vol. 123, no. 18. — P. 9992–10022. — https://doi.org/10.1029/2017JD028250.

Fritts D. C., Wang L., Taylor M. J., et al. Large-Amplitude Mountain Waves in the Mesosphere Observed on 21 June 2014 During DEEPWAVE: 2. Nonlinear Dynamics, Wave Breaking, and Instabilities // Journal of Geophysical Research: Atmospheres. — 2019. — Vol. 124, no. 17/18. — P. 10006–10032. — https://doi.org/10.1029/2019jd030899.

Gavrilov N. M. Parametrization of the dynamical and thermal effect of steadystate internal gravity waves on the middle atmosphere // Izvestiya Atmospheric and Oceanic Physics. — 1989. — Vol. 25, no. 3. — P. 271–278. — (In Russian).

Gavrilov N. M. and Koval A. V. Parameterization of mesoscale stationary orographic wave forcing for use in numerical models of atmospheric dynamics // Izvestiya, Atmospheric and Oceanic Physics. — 2013. — Vol. 49, no. 3. — P. 244–251. — https://doi.org/10.1134/s0001433813030067.

Gavrilov N. M., Koval A. V., Pogoreltsev A. I., et al. Numerical simulation of the response of general circulation of the middle atmosphere to spatial inhomogeneities of orographic waves // Izvestiya, Atmospheric and Oceanic Physics. — 2013. — Vol. 49, no. 4. — P. 367–374. — https://doi.org/10.1134/S0001433813040038.

Gavrilov N. M., Koval A. V., Pogoreltsev A. I., et al. Simulating influences of QBO phases and orographic gravity wave forcing on planetary waves in the middle atmosphere // Earth, Planets and Space. — 2015. — Vol. 67, no. 1. — https://doi.org/10.1186/s40623-015-0259-2.

Gavrilov N. M., Koval A. V., Pogoreltsev A. I., et al. Simulating planetary wave propagation to the upper atmosphere during stratospheric warming events at different mountain wave scenarios // Advances in Space Research. — 2018. — Vol. 61, no. 7. — P. 1819–1836. — https://doi.org/10.1016/j.asr.2017.08.022.

Gavrilov N. M. and Kshevetskii S. P. Numerical modeling of the propagation of nonlinear acoustic-gravity waves in the middle and upper atmosphere // Izvestiya, Atmospheric and Oceanic Physics. — 2014. — Vol. 50, no. 1. — P. 66–72. — https://doi.org/10.1134/s0001433813050046.

Gavrilov N. M. and Popov A. A. Modeling Seasonal Variations in the Intensity of Internal Gravity Waves in the Lower Thermosphere // Izvestiya, Atmospheric and Oceanic Physics. — 2022. — Vol. 58, no. 1. — P. 68–79. — https://doi.org/10.1134/s0001433822010030.

Geleyn J. F., Balize E., Bougeault P., et al. Atmospheric parametrization schemes in Meteo-France's ARPEGE N.W.P. model // Seminar on Parametrization of Sub-grid Scale Physical Processes. — ECMWF, 1994. — P. 385–402.

Gossard E. E. and Hooke W. H. Waves in the atmosphere. Atmospheric Infrasound and Gravity Waves - their Generation and Propagation. — Amsterdam, Oxford, NY : Elsevier Scientific Publishing Company, 1975. — 456 p.

Hájková D. and Šácha P. Parameterized orographic gravity wave drag and dynamical effects in CMIP6 models // Climate Dynamics. — 2023. — Vol. 62, no. 3. — P. 2259–2284. — https://doi.org/10.1007/s00382-023-07021-0.

Heale C. J., Bossert K., Vadas S. L., et al. Secondary Gravity Waves Generated by Breaking Mountain Waves Over Europe // Journal of Geophysical Research: Atmospheres. — 2020. — Vol. 125, no. 5. — https://doi.org/10.1029/2019JD031662.

Hegglin M. I., Lamarque J. F. and Eyring V. The IGAC/SPARC Chemistry-Climate Model Initiative Phase-1 (CCMI-1) model data output. — 2015. — URL: https://catalogue.ceda.ac.uk/uuid/9cc6b94df0f4469d8066d69b5df879d5/ (visited on 01/15/2025).

Hoffmann L., Xue X. and Alexander M. J. A global view of stratospheric gravity wave hotspots located with Atmospheric Infrared Sounder observations // Journal of Geophysical Research: Atmospheres. — 2013. — Vol. 118, no. 2. — P. 416–434. — https://doi.org/10.1029/2012jd018658.

Iwasaki T., Yamada S. and Tada K. A Parameterization Scheme of Orographic Gravity Wave Drag with Two Different Vertical Partitionings: Part I: Impacts on Medium-Range Forecasts // Journal of the Meteorological Society of Japan. Ser. II. — 1989. — Vol. 67, no. 1. — P. 11–27. — https://doi.org/10.2151/jmsj1965.67.1_11.

Jucker M. Scaling of Eliassen-Palm flux vectors // Atmospheric Science Letters. — 2021. — Vol. 22, no. 4. — https://doi.org/10.1002/asl.1020.

Kaifler B., Kaifler N., Ehard B., et al. Influences of source conditions on mountain wave penetration into the stratosphere and mesosphere // Geophysical Research Letters. — 2015. — Vol. 42, no. 21. — P. 9488–9494. — https://doi.org/10.1002/2015GL066465.

Koval A. V., Chen W., Didenko K. A., et al. Modelling the residual mean meridional circulation at different stages of sudden stratospheric warming events // Annales Geophysicae. — 2021. — Vol. 39, no. 2. — P. 357–368. — https://doi.org/10.5194/angeo-39-357-2021.

Koval A. V., Gavrilov N. M., Kandieva K. K., et al. Numerical simulation of stratospheric QBO impact on the planetary waves up to the thermosphere // Scientific Reports. — 2022. — Vol. 12, no. 1. — https://doi.org/10.1038/s41598-022-26311-x.

Koval A. V., Gavrilov N. M., Pogoreltsev A. I., et al. Numerical simulation of the mean meridional circulation in the middle atmosphere at different phases of stratospheric warmings and mountain wave scenarios // Journal of Atmospheric and Solar-Terrestrial Physics. — 2019a. — Vol. 183. — P. 11–18. — https://doi.org/10.1016/j.jastp.2018.12.012.

Koval A. V., Gavrilov N. M., Pogoreltsev A. I., et al. Reactions of the Middle Atmosphere Circulation and Stationary Planetary Waves on the Solar Activity Effects in the Thermosphere // Journal of Geophysical Research: Space Physics. — 2019b. — Vol. 124, no. 12. — P. 10645–10658. — https://doi.org/10.1029/2019ja027392.

Koval A. V., Gavrilov N. M., Zubov V. A., et al. Modified Parameterization Scheme of Orographic Gravity Waves in the SOCOL Chemistry-Climate Model // Pure and Applied Geophysics. — 2024. — Vol. 182, no. 1. — P. 255–270. — https://doi.org/10.1007/s00024-024-03619-5.

Lilly D. K. and Kennedy P. J. Observations of a Stationary Mountain Wave and its Associated Momentum Flux and Energy Dissipation // Journal of the Atmospheric Sciences. — 1973. — Vol. 30, no. 6. — P. 1135–1152. — https://doi.org/10.1175/1520-0469(1973)030<1135:ooasmw>2.0.co;2.

Lott F. and Miller M. J. A new subgrid-scale orographic drag parametrization: Its formulation and testing // Quarterly Journal of the Royal Meteorological Society. — 1997. — Vol. 123, no. 537. — P. 101–127. — https://doi.org/10.1002/qj.49712353704.

McFarlene N. The Effect of Orographically Excited Gravity Wave Drag on the General Circulation of the Lower Stratosphere and Troposphere // Journal of the Atmospheric Sciences. — 1987. — Vol. 44, no. 14. — P. 1775–1800. — https://doi.org/10.1175/1520-0469(1987)044<1775:teooeg>2.0.co;2.

Niekerk A. van, Sandu I. and Vosper S. B. The Circulation Response to Resolved Versus Parametrized Orographic Drag Over Complex Mountain Terrains // Journal of Advances in Modeling Earth Systems. — 2018. — Vol. 10, no. 10. — P. 2527–2547. — https://doi.org/10.1029/2018ms001417.

Niekerk A. van, Sandu I., Zadra A., et al. COnstraining ORographic Drag Effects (COORDE): A Model Comparison of Resolved and Parametrized Orographic Drag // Journal of Advances in Modeling Earth Systems. — 2020. — Vol. 12, no. 11. — https://doi.org/10.1029/2020ms002160.

NOAA National Geophysical Data Center. 2-minute Gridded Global Relief Data (ETOPO2) v2. — 2006. — https://doi.org/10.7289/V5J1012Q.

Roeckner E., Bäuml G., Bonaventura L., et al. Report No 349. The atmospheric general circulation model ECHAM5. Part I. Model description. — Hamburg, Germany : Max Planck Institute for Meteorology, 2003.

Schraner M., Rozanov E., Schnadt Poberaj C., et al. Technical Note: Chemistry-climate model SOCOL: version 2.0 with improved transport and chemistry/microphysics schemes // Atmospheric Chemistry and Physics. — 2008. — Vol. 8, no. 19. — P. 5957–5974. — https://doi.org/10.5194/acp-8-5957-2008.

Scinocca J. F. and McFarlane N. A. The parametrization of drag induced by stratified flow over anisotropic orography // Quarterly Journal of the Royal Meteorological Society. — 2000. — Vol. 126, no. 568. — P. 2353–2393. — https://doi.org/10.1002/qj.49712656802.

Smith R. B., Woods B. K., Jensen J., et al. Mountain Waves Entering the Stratosphere // Journal of the Atmospheric Sciences. — 2008. — Vol. 65, no. 8. — P. 2543–2562. — https://doi.org/10.1175/2007jas2598.1.

Smith S., Baumgardner J. and Mendillo M. Evidence of mesospheric gravity-waves generated by orographic forcing in the troposphere // Geophysical Research Letters. — 2009. — Vol. 36, no. 8. — https://doi.org/10.1029/2008gl036936.

Stenke A., Schraner M., Rozanov E., et al. The SOCOL version 3.0 chemistry-climate model: description, evaluation, and implications from an advanced transport algorithm // Geoscientific Model Development. — 2013. — Vol. 6, no. 5. — P. 1407–1427. — https://doi.org/10.5194/gmd-6-1407-2013.

Swinbank R. and O'Neill A. A Stratosphere-Troposphere Data Assimilation System // Monthly Weather Review. — 1994. — Vol. 122, no. 4. — P. 686–702. — https://doi.org/10.1175/1520-0493(1994)122<0686:astdas>2.0.co;2.

Tables of Physical Quantities / ed. by I. K. Kikoin. — Moscow : Atomizdat, 1976. — P. 272–279. — (In Russian).

Webster S., Brown A. R., Cameron D. R., et al. Improvements to the representation of orography in the Met Office Unified Model // Quarterly Journal of the Royal Meteorological Society. — 2003. — Vol. 129, no. 591. — P. 1989–2010. — https://doi.org/10.1256/qj.02.133.

Zadra A., Roch M., Laroche S., et al. The subgrid-scale orographic blocking parametrization of the GEM Model // Atmosphere-Ocean. — 2003. — Vol. 41, no. 2. — P. 155–170. — https://doi.org/10.3137/ao.410204.

Zhao M., Golaz J. C., Held I. M., et al. The GFDL Global Atmosphere and Land Model AM4.0/LM4.0: 2. Model Description, Sensitivity Studies, and Tuning Strategies // Journal of Advances in Modeling Earth Systems. — 2018. — Vol. 10, no. 3. — P. 735–769. — https://doi.org/10.1002/2017ms001209.